

## REVEALING THE HOST GALAXY OF A QUASAR 2175 Å DUST ABSORBER AT $Z = 2.12$

JINGZHE MA<sup>1,2</sup>, GABRIEL BRAMMER<sup>3</sup>, JIAN GE<sup>1</sup>, J. XAVIER PROCHASKA<sup>4</sup>, AND BRITT LUNDGREN<sup>5</sup>

*Draft version March 22, 2022*

### ABSTRACT

We report the first detection of the host galaxy of a strong 2175 Å dust absorber at  $z = 2.12$  towards the background quasar SDSS J121143.42+083349.7 using *HST*/WFC3 IR F140W direct imaging and G141 grism spectroscopy. The spectroscopically confirmed host galaxy is located at a small impact parameter of  $\sim 5.5$  kpc ( $\sim 0.65''$ ). The F140W image reveals a disk-like morphology with an effective radius of  $2.24 \pm 0.08$  kpc. The extracted 1D spectrum is dominated by a continuum with weak emission lines ([O III] and [O II]). The [O III]-based unobscured star formation rate (SFR) is  $9.4 \pm 2.6 M_{\odot} \text{yr}^{-1}$  assuming an [O III]/H $\alpha$  ratio of 1. The moderate 4000 Å break (D<sub>n</sub>(4000) index  $\sim 1.3$ ) and Balmer absorption lines indicate that the host galaxy contains an evolved stellar population with an estimated stellar mass  $M_*$  of  $(3 - 7) \times 10^{10} M_{\odot}$ . The SFR and  $M_*$  of the host galaxy are comparable to, though slightly lower than, those of typical emission-selected galaxies at  $z \sim 2$ . As inferred from our absorption analysis in Ma et al. (2015, 2017, 2018), the host galaxy is confirmed to be a chemically-enriched, evolved, massive, and star-forming disk-like galaxy that is likely in the transition from a blue star-forming galaxy to a red quiescent galaxy.

*Keywords:* galaxies: high-redshift - quasars: absorption lines

### 1. INTRODUCTION

Absorption line systems towards bright background quasars or gamma-ray burst afterglows provide excellent probes of the gas in and around galaxies irrespective of their luminosities. The absorber-galaxy relation is established by detecting the emission counterparts of absorption systems. The searches for emission counterparts of the extensively studied damped Lyman- $\alpha$  absorbers (DLAs) and Mg II absorbers have been conducted for more than two decades (see recent reviews Krogager et al. 2017; Joshi et al. 2017). The picture of what types of galaxies hosting these absorbers is emerging with an increased number of detections, although the detection rate remains very low largely due to the fact that the absorber's host tends to be too faint or too close in angular separation to the bright quasar. DLA counterparts found in emission have properties overlapping with Lyman- $\alpha$  emitters (LAEs), Lyman break galaxies (LBGs), and dwarf galaxies (e.g., Fynbo et al. 2008; Rauch et al. 2008; Krogager et al. 2013; Fumagalli et al. 2015; Neeleman et al. 2017). A more general paradigm is that DLAs trace star-forming galaxies with a large span of masses, luminosities, and star formation rates (SFRs). Mg II absorbers are found to be associated with either galactic-scale outflows originating from their host galaxies (Bouché et al. 2006; Lundgren et al. 2012; Bordoloi et al. 2014), dynamical mergers or filamentary accretion onto galaxies (Steidel et al. 2002; Chen et al. 2010; Rubin

et al. 2012), or high-velocity clouds (Richter 2012; Herenz et al. 2013). Therefore Mg II absorbers can be used to trace many different feedback processes regulating the evolution of their host galaxies (Joshi et al. 2017).

A new population of quasar absorption systems beyond the local Universe, 2175 Å dust absorbers (2DAs; the broad absorption feature centered around rest-frame 2175 Å commonly seen in the Milky Way extinction curves; e.g. Wang et al. 2004; Srianand et al. 2008; Jiang et al. 2011), and its relationships with other absorption line systems (e.g., DLAs, Mg II absorbers) has been established (Ma et al. 2018). These absorbers contain signatures of not only gas but also dust in the absorbing galaxies (Ma et al. 2017, 2018). 2DAs are a subset of Mg II (and Fe II) absorbers. Compared with DLAs or subDLAs in the literature, the 2DAs on average have higher metallicities, higher depletion levels (onto dust), and larger velocity widths, indicating higher stellar masses (with an estimated median value of  $\sim 2 \times 10^{10} M_{\odot}$ ; Ma et al. 2018). They are more likely to be drawn from the same parent population as metal-strong DLAs/subDLAs, which are defined as having  $\log N(\text{Zn II}/\text{cm}^{-2}) \geq 13.15$  or  $\log N(\text{Si II}/\text{cm}^{-2}) \geq 15.95$  (Herbert-Fort et al. 2006). In addition to a great number of low ionization lines (e.g., Zn II, Mg II, Fe II, Si II, Al II, Ni II, Mn II, Ca II, Ti II) detected in 2DAs, neutral C I lines are detected in all of the 2DAs (as long as covered in the spectra) with  $\log N(\text{C I}/\text{cm}^{-2}) > 14.0$  (Ma et al. 2018). Given the relatively high metallicity and the presence of C I, 2DAs can be used as molecular gas tracers, and the simultaneous presence of the 2175 Å bump and molecular gas (H<sub>2</sub> and/or CO) has been reported in a few absorbers (e.g., Noterdaeme et al. 2009; Prochaska et al. 2009; Ma et al. 2015; Noterdaeme et al. 2017).

All the pieces of evidence suggest that the host galaxies are likely to be chemically enriched, evolved, massive

<sup>1</sup> Department of Astronomy, University of Florida, Gainesville, FL 32611, USA

<sup>2</sup> Department of Physics & Astronomy, University of California, Irvine, CA 92617, USA; jingzhem@uci.edu

<sup>3</sup> Space Telescope Science Institute, 3700 San Martin Dr, Baltimore, MD 21211, USA

<sup>4</sup> Department of Astronomy and Astrophysics, UCO/Lick Observatory, University of California, 1156 High Street, Santa Cruz, CA 95064, USA

<sup>5</sup> Department of Physics, University of North Carolina, Asheville, NC 28804, USA

(more massive than typical DLA/subDLA galaxies), and presumably star-forming galaxies given the neutral and molecular gas in the systems. To establish the absorber-galaxy relation for 2DAs and obtain fundamental galaxy properties such as star formation rate (SFR) and stellar mass, we need to reveal the host galaxies in emission. The emission counterparts of 2DAs are expected to be detected more easily than typical DLAs/subDLAs (Ma et al. 2018). Confirming the emission counterparts of 2DAs is essential to placing this population in the context of galaxy populations in general. Upon establishing this association, we may leverage the exquisite measurements of these 2DAs to examine the chemically mature interstellar medium (ISM) of galaxies in the  $z \sim 2$  universe.

The strong 2DA at  $z = 2.1166$  towards QSO J121143.42+083349.7 ( $z = 2.4828$ , hereafter J1211+0833) from the Sloan Digital Sky Survey Data Release 10 stands out as an excellent target for revealing the host galaxy in emission. It is classified as a solar-metallicity DLA and a Mg II (and Fe II) absorber with the remarkably simultaneous presence of C I, CO and neutral chlorine (Cl I; a tracer of  $H_2$ ). The chemical abundances and physical conditions are characterized in detail in Ma et al. (2015).

In this Letter, we report the detection of the host galaxy of this 2DA using *HST*/WFC3 IR direct imaging and slitless spectroscopy. Section 2 and Section 3 describe the observations and data reduction processes that lead to the confirmation of the galaxy redshift. We discuss the properties derived from the *HST* data in Section 4 and summarize the results in Section 5. Throughout this paper, we assume a flat  $\Lambda$ CDM cosmological model with  $H_0 = 70 \text{ km s}^{-1} \text{ Mpc}^{-1}$ ,  $\Omega_M = 0.3$ , and  $\Omega_\Lambda = 0.7$ .

## 2. OBSERVATIONS AND INITIAL DATA REDUCTION

The WFC3 G141 grism has spectral coverage from 1.1 to  $1.65 \mu\text{m}$  with a dispersion of  $46.5 \text{ \AA pixel}^{-1}$  ( $R \sim 130$ ) in the primary spectral order before drizzling. Thus, the grism observations cover the rest-frame Balmer break, 4000  $\text{\AA}$  break, 3727  $\text{\AA}$  [O II],  $H\beta$ , and 4959 and 5007  $\text{\AA}$  [O III] features at the redshift of the absorber’s host galaxy.

This target was observed with paired F140W direct imaging and G141 grism in three visits (one orbit per visit) on 15 November 2015, 24 December 2015, and 26 February 2016 with dispersion position angles,  $75^\circ$ ,  $55^\circ$ , and  $26^\circ$  east of north, respectively (GO 14200, PI: J. Ma). Two dithered pairs of direct (F140W, 465 s) and grism (G141, 2206 s) images were obtained. The direct images are used for source identification (Figure 1) and wavelength calibration of the slitless spectra.

The direct imaging and grism data were reduced together using the “Grism redshift & line” analysis software for space-based slitless spectroscopy (Grizli<sup>6</sup>; Brammer et al. in preparation). The end-to-end processing of the data includes four major steps: (1) pre-processing of FLT files downloaded from MAST, (2) field contamination modeling, (3) spectral extractions, (4) redshift and continuum & emission line fitting. The pre-processing involves astrometric registration, grism sky background

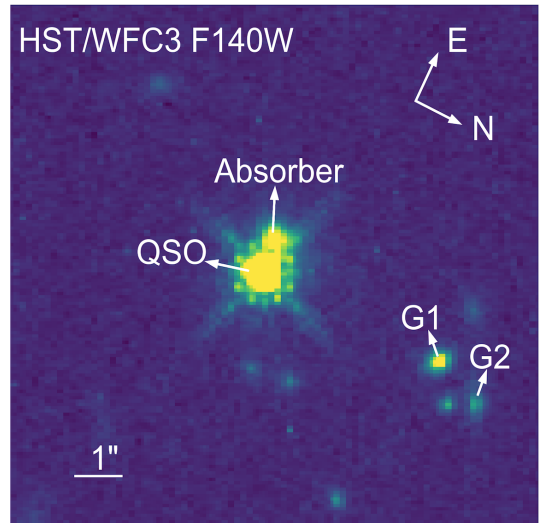


**Figure 1.** *HST*/WFC3 F140W image. The host galaxy of the J1211+0833 absorber is revealed  $\sim 0.65''$  from the quasar sightline. G1 and G2 are two nearby galaxies at  $z = 2.1188$  and  $z = 2.2433$ , respectively.

subtraction & flat-fielding, and extracting visit-level catalogs and segmentation images from the direct imaging (Brammer et al. 2012). The products of this step are aligned, background-subtracted FLTs and drizzled mosaics of direct and grism images ( $0.06'' \text{ pixel}^{-1}$ ).

The absorber’s host galaxy was expected to lie close to the quasar sightline given its strong absorption lines ( $W_r(\lambda 2796) = 2.43 \pm 0.06 \text{ \AA}$ ), based on the known anticorrelation between Mg II equivalent widths and impact parameters (Chen et al. 2010; Nielsen et al. 2013a and references therein). Figure 1 shows the F140W image where the scale is stretched to reveal a companion very close to the quasar sightline (projected distance  $\sim 0.65''$ ), being the best candidate for the host galaxy of the J1211+0833 absorber. Several objects are also present in the same field within  $\sim 5''$  ( $\sim 42 \text{ kpc}$  at  $z_{\text{abs}}$ ) of the quasar. The next steps are to remove contaminations and extract 1D spectra to derive the redshifts of the close companion and nearby objects.

## 3. CONTAMINATION MODELING, SPECTRAL EXTRACTION, AND REDSHIFT CONFIRMATION

Due to the close proximity of the bright quasar, it is critical to model and subtract the quasar contamination. To model the 2D spectrum of the quasar or any given object in the direct image, we first compute the trace and dispersion parameters that define the mapping of a single pixel in the reference (direct) image into a one-pixel-wide spectrum in the dispersed image (i.e., the 2D grism image). The full 2D model is generated by shifting and adding this elemental spectrum scaled by the observed brightness in the direct image (Brammer et al. 2012; Momcheva et al. 2016).

We use the effective point spread function (ePSF<sup>7</sup>; Anderson 2016) to model the quasar direct image and use the templates in the Grizli database to fit and subtract the 2D PSF trace iteratively. The top panel in Figure 2 displays the residuals after subtracting the quasar in each visit (first three rows). The quasar-subtracted di-

<sup>6</sup> <https://github.com/gbrammer/grizli/>

<sup>7</sup> <http://www.stsci.edu/hst/wfc3/analysis/PSF>

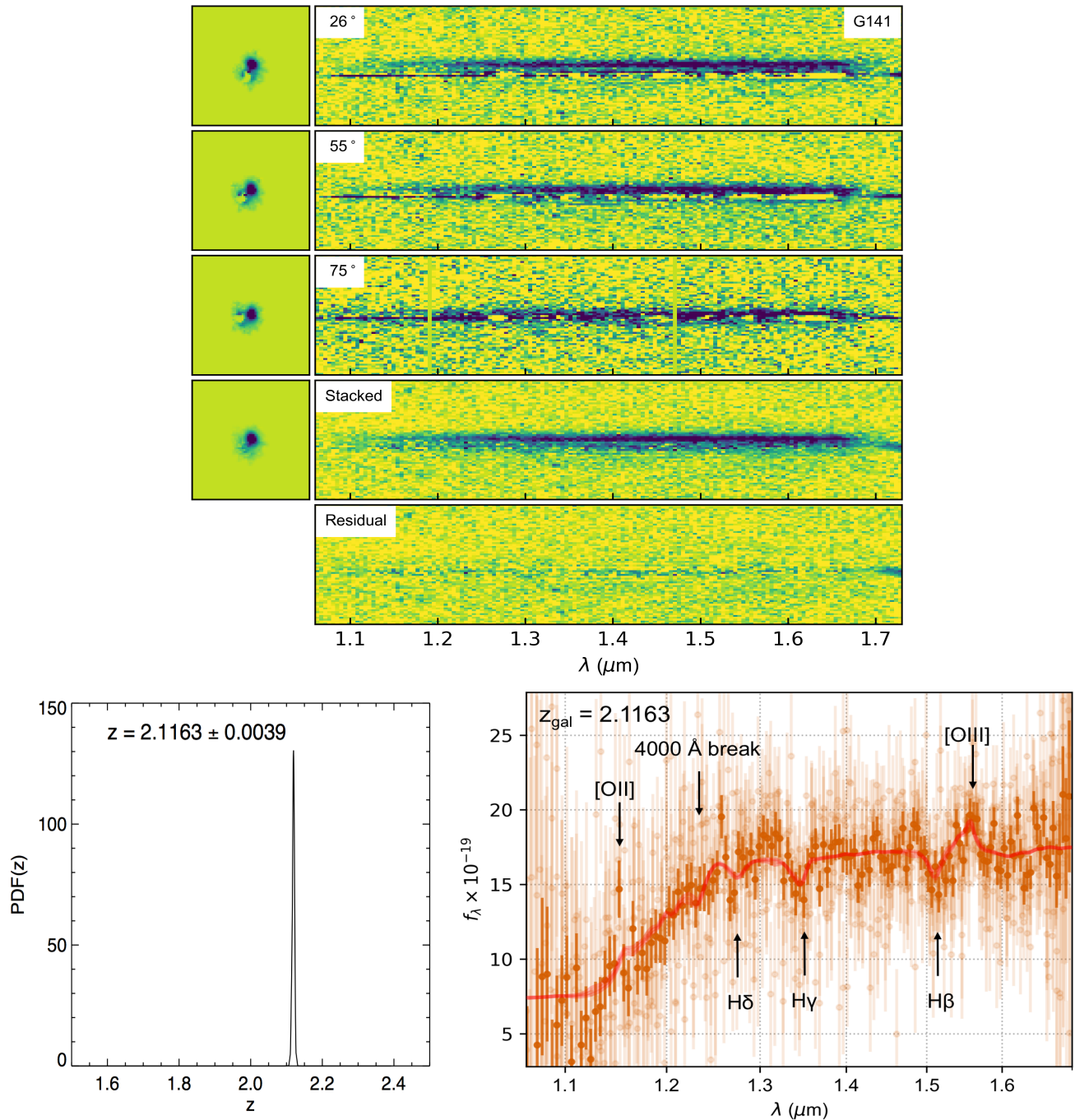


**Figure 2.** *Top:* The first three rows show the residuals after subtracting the quasar in F140W (left) and G141 (right) in each visit. The dispersion position angles for the three visits are  $26^\circ$ ,  $55^\circ$ , and  $75^\circ$  respectively. The fourth row shows the stacked image (left) and stacked 2D grism spectrum (right). The last row shows the overall residuals after subtracting the best-fit 2D spectrum for the host galaxy. *Bottom Left:* The redshift probability distribution. The best-fit redshift is at  $z = 2.1163$ . *Bottom Right:* The extracted 1D spectrum for the 2DA host galaxy. The faint orange data points display the 1D spectra extracted from each of the six individual grism exposures, and the red curve is the best-fit template to the binned data (dark orange; binned to the native pixel scale of  $46.5 \text{ \AA pixel}^{-1}$ ).

rect and grism images from the three visits are re-drizzled for modeling the companion’s 2D spectrum. The fourth row displays the stacked image and 2D spectrum from the three visits. The last row shows the reasonably clean residuals (the positive pixels are due to the residuals from the quasar subtraction) after subtracting the best-fit model for the companion. We determine the companion redshift by fitting the Flexible Stellar Population Synthesis templates (FSPS; Conroy et al. 2009; Conroy &

Gunn 2010) to the quasar-subtracted exposure-level 2D spectra over a grid of redshifts. The bottom left panel of Figure 2 shows the result of this fit, indicating a prominent peak with maximum posterior probability of  $z = 2.1163 \pm 0.0039$ , which is in excellent agreement with the redshift of the 2DA ( $\Delta z = z_{gal} - z_{abs} = 0.0003$ ). This close companion is indeed responsible for the strong 2DA. The bottom right panel shows an optimal 1D extraction (Horne 1986) of the companion spectrum (or-

ange points with uncertainties) and the best-fit FSPS model at the derived redshift (red curve). The properties of the rest-frame optical spectrum of the absorber, which shows a continuum break and Balmer absorption lines, is discussed in more detail in Section 4.4.

We further extract spectra and fit redshifts for the nearby objects in the same manner. G1 and G2 are at redshifts close to the companion’s redshift ( $z_{G1} = 2.1188 \pm 0.0064$ ,  $z_{G2} = 2.2433 \pm 0.0032$ ). We have checked the deep VLT/UVES spectrum (Ma et al. 2015) but no absorption features were found for these two galaxies.

#### 4. DISCUSSION

We have demonstrated that the high-resolution *HST* imaging successfully recovers the absorber’s host galaxy and enables extraction of the grism spectrum to confirm the redshift. The direct imaging and grism spectroscopy provide ample information about the properties of the host galaxy (Table 1), including the impact parameter, morphology, SFR, SFR surface density, and stellar mass. These are the fundamental parameters that can be used to compare with other absorption-selected galaxies (e.g., DLAs, Mg II absorbers) and place this population in context with the well-established galaxy populations in emission.

##### 4.1. Morphology

We perform surface brightness profile fitting on the F140W image using GALFIT (Peng et al. 2010). We derive the effective radius ( $R_e$ ), Sérsic index ( $n$ ), and axis ratio ( $b/a$ ). The measurements and uncertainties from GALFIT are presented in Table 1. The Sérsic index of  $0.92 \pm 0.10$  is consistent with a disk morphology. The effective radius from GALFIT is along the semi-major axis, and we convert it to a circularized effective radius  $R_{e,c} = R_e \sqrt{b/a} = 1.91 \pm 0.08$  kpc using the measured axis ratio of  $0.73 \pm 0.03$ . These morphological parameters are in the range of the values of the  $z > 1$  DLA and Mg II galaxies in the literature (Lundgren et al. 2012; Krogager et al. 2013).

##### 4.2. Impact parameter

###### 4.2.1. $W_r(\lambda 2796)$ and impact parameter

The anti-correlation between the rest-frame equivalent width of Mg II absorption and the impact parameter has been well-established (e.g., Bergeron & Boissé 1991; Steidel 1995; Chen et al. 2010; Rao et al. 2011; Nielsen et al. 2013a,b), albeit with a large scatter. Chen et al. (2010) describes the relation using a simple power-law, while Nielsen et al. (2013a,b) have shown a  $7.9\sigma$  anti-correlation well represented by a log-linear relation. Figure 3 shows the individual measurements at  $0.10 < z < 2.35$  in the literature and the best-fit relations by Chen et al. (2010) and Nielsen et al. (2013a,b).

The host galaxy of the J1211+0833 2DA is located at an impact parameter of 5.5 kpc, which is the smallest angular separation among the Mg II absorbers at  $z > 2$  directly detected and spectroscopically confirmed in emission. This absorber presents ultra-strong Mg II absorption lines ( $W_r(\lambda 2796) = 2.43 \pm 0.06$  Å; Ma et al. 2015) in close agreement with the power-law relation obtained by Chen et al. (2010).

###### 4.2.2. $N(H\text{ I})$ and impact parameter

The right panel in Figure 3 displays  $N(H\text{ I})$  as a function of impact parameter of DLA and subDLAs for the spectroscopically confirmed absorbing galaxies compiled by Rahmani et al. (2016). The DLAs/subDLAs at  $z > 1$  on average show higher  $N(H\text{ I})$  and smaller impact parameters than those at  $z < 1$ . At impact parameters higher than 20 kpc, there are no DLAs with  $\log N(H\text{ I}/\text{cm}^{-2}) > 21.0$ . The host galaxy of the 2DA is located among the ones with high  $N(H\text{ I})$  and small impact parameters. A few high- $z$  DLA galaxies are detected at very small impact parameters ( $< 5$  kpc; Møller & Warren 1993; Krogager et al. 2012; Noterdaeme et al. 2012).

##### 4.3. SFR and SFR surface density

The overall shape of the extracted grism spectrum is dominated by a continuum with a prominent Balmer/4000 Å break and weak emission lines, [O III] $\lambda 5007$  and [O II] $\lambda 3727$ . We measure the line fluxes to be  $(6.2 \pm 1.7) \times 10^{-17}$  erg  $\text{s}^{-1} \text{cm}^{-2}$  for [O III] and  $< 7.9 \times 10^{-17}$  erg  $\text{s}^{-1} \text{cm}^{-2}$  ( $3\sigma$  upper limit) for [O II]. Emission line fluxes are determined from the normalization of the emission line templates, and their uncertainties are derived from the covariance matrix of the 2D template models weighted by the pixel variances.

[O II] and [O III] have been used as SFR indicators whenever  $H\alpha$  is not available, albeit with uncertainties as large as a factor of 2-4. We convert the [O III] luminosity (assuming [O III]/ $H\alpha = 1$ ) to SFR using the  $H\alpha$ -based SFR calibration of Kennicutt (1998) converted to a Chabrier (2003) initial mass function (IMF),  $\text{SFR} (M_{\odot} \text{yr}^{-1}) = 4.4 \times 10^{-42} L_{H\alpha} / \text{erg s}^{-1} = 9.4 \pm 2.6 M_{\odot} \text{yr}^{-1}$ . The [O II]-based SFR is calculated as  $\text{SFR} (M_{\odot} \text{yr}^{-1}) = 7.8 \times 10^{-42} L_{[OII]} / \text{erg s}^{-1} < 21 M_{\odot} \text{yr}^{-1}$  ( $3\sigma$  upper limit). This SFR is in the range of the SFRs of Mg II host galaxies at  $z \sim 2$  with  $W_r(\lambda 2796) > 2$  Å (Bouché et al. 2012; Lundgren et al. 2012). We compare the SFRs of Mg II and H I galaxies with emission-selected galaxies at  $z \sim 2-3$  in Figure 4. The J1211+0833 2DA’s host galaxy has a SFR significantly higher than most of the DLA/subDLA galaxies and lies between the median values of LAEs and LBGs.

We further calculate the SFR surface density given the size measurement from the F140W imaging as

$$\Sigma \text{SFR} (M_{\odot} \text{yr}^{-1} \text{kpc}^{-2}) = \text{SFR} / (2\pi R_{e,c}^2) \quad (1)$$

where  $R_{e,c}$  is the circularized effective radius of the host galaxy. The  $\Sigma \text{SFR}$  is within the range of the Mg II host galaxies in Lundgren et al. (2012).

##### 4.4. $D_n(4000)$ , age, stellar mass, Virial radius, and star formation history

The break at 4000 Å arises because of the accumulation of a large number of metal lines in a narrow wavelength region. The strength of the 4000 Å break is measured as the flux ratio between the wavelength windows adjacent to the 4000 Å break. We use the  $D_n(4000)$  index defined as the ratio between 3850-3950 Å and 4000 - 4100 Å (Balogh et al. 1999). The  $D_n(4000)$  index increases as

**Table 1**  
Properties of the J1211+0833 absorber’s host galaxy

<i>HST</i> /WFC3 F140W	
Coordinate (RA; Dec)	12:11:43.44, +08:33:49.5
Magnitude (AB)	$21.56 \pm 0.10$
Sérsic index (n)	$0.92 \pm 0.10$
Effective semi-major axis ( $R_e$ )	$0.27 \pm 0.01''$ or $2.24 \pm 0.08$ kpc
Circularized effective radius ( $R_{e,c}$ )	$1.91 \pm 0.08$ kpc
Axis ratio (b/a)	$0.73 \pm 0.03$
Impact parameter (D)	5.5 kpc
<i>HST</i> /WFC3 G141	
Galaxy redshift ( $z_{gal}$ )	$2.1163 \pm 0.0039$
[OIII] line flux	$(6.2 \pm 1.7) \times 10^{-17}$ erg s $^{-1}$ cm $^{-2}$
[OII] line flux $3\sigma$ upper limit	$< 7.9 \times 10^{-17}$ erg s $^{-1}$ cm $^{-2}$
Unobscured SFR (Chabrier IMF)	$9.4 \pm 2.6$ M $_{\odot}$ yr $^{-1}$
$\Sigma_{SFR}$	$0.4 \pm 0.1$ M $_{\odot}$ yr $^{-1}$ kpc $^{-2}$
$M_*$	$(3 - 7) \times 10^{10}$ M $_{\odot}$

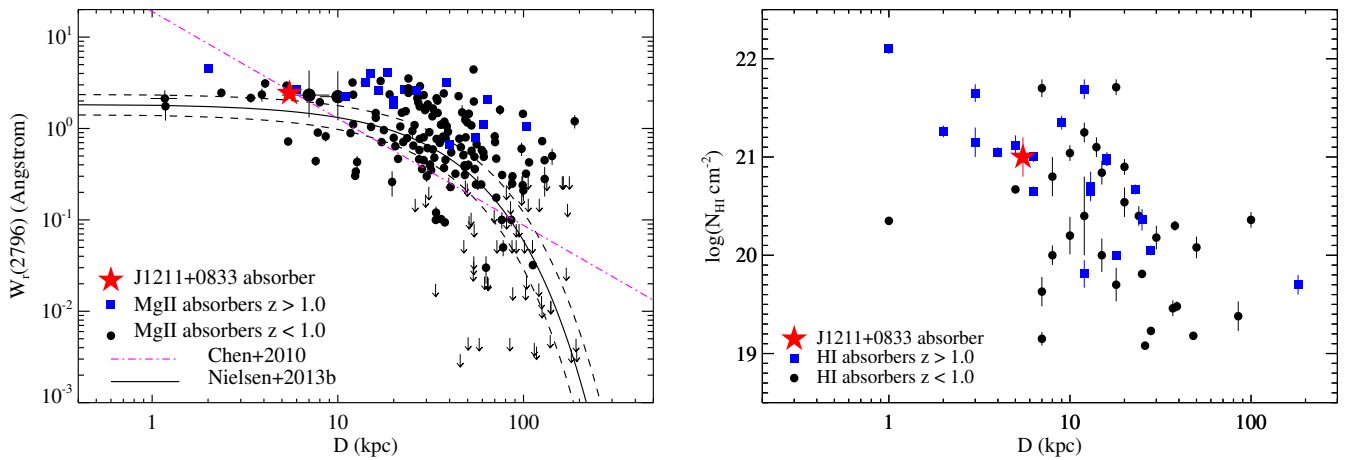


**Figure 3.** *Left:* Observed anti-correlation between the rest-frame equivalent width of Mg II absorption,  $W_r(\lambda 2796)$ , and galaxy impact parameter,  $D$ . The individual measurements from the literature include Bouché et al. (2007, 2012), Lundgren et al. (2012), Nielsen et al. (2013a), Kacprzak et al. (2013), and Joshi et al. (2017). The pink dash-dotted line is the power-law fit obtained by Chen et al. (2010). The solid curve is a log-linear maximum likelihood fit given by Nielsen et al. (2013b) with the associated  $1\sigma$  denoted by the dashed curves. *Right:* Anti-correlation between  $\log N(\text{H I})$  and impact parameter. The black circles and blue squares are the detected DLA and subDLA host galaxies in the literature at  $z < 1$  and  $z > 1$  respectively, compiled by Rahmani et al. (2016).

a function of stellar population age and provide a characteristic age for the galaxy (Kauffmann et al. 2003a). We measure a  $Dn(4000)$  index for the 2DA host galaxy of  $1.3 \pm 0.3$ , indicating the stellar population is about 1 Gyr old. We estimate the stellar mass to be in the range of  $\log(M_*/M_{\odot}) = 10.5 - 10.8$  based on two correlations: the  $Dn(4000)$ -stellar mass relation (Kauffmann et al. 2003b; Hernán-Caballero et al. 2013) and the mass-size relation (Krogager et al. 2014). This stellar mass is within the range predicted by the stellar mass estimators based on absorption properties (Equations 5 & 6 in Ma et al. 2018). Since we only have one photometric data point at F140W and a narrow window of spectral coverage, multi-wavelength spectral energy distribution modeling with more photometric and/or spectral coverage would improve the estimates. We further convert the stellar mass to halo mass (Behroozi et al. 2013) to derive the Virial radius of the host galaxy halo to be  $\sim 80 - 100$  kpc. The background quasar is already probing the ISM of the 2DA host galaxy while most quasar absorption line systems trace the circumgalactic or intergalactic medium.

The [O III] and [O II] emission lines, although weak, suggest ongoing star formation in the host galaxy. On the other hand, moderate Balmer absorption lines are also present in the spectrum, which are signs of increased fraction of A or F type stars in a recent starburst. The type of galaxy hosting the 2DA emerges as being in the transition from a star-forming galaxy to a quiescent galaxy where star formation has been quenched. Galaxies caught in the act of transition are either in the final stage of a starburst or have recently quenched star formation, and the so-called post-starburst galaxies are one such class (Wild et al. 2016). The J1211+0833 absorber’s host galaxy is likely in the early stage of transition, i.e., the final starburst phase.

A coherent picture of the 2DA host galaxy has been pieced together with the properties derived from the absorption analysis (Ma et al. 2015, 2017, 2018) and the emission counterpart studied in this work: The host galaxy is indeed a chemically-enriched, evolved, massive, and star-forming disk-like galaxy, although it is likely in the final stage of star formation and is tran-

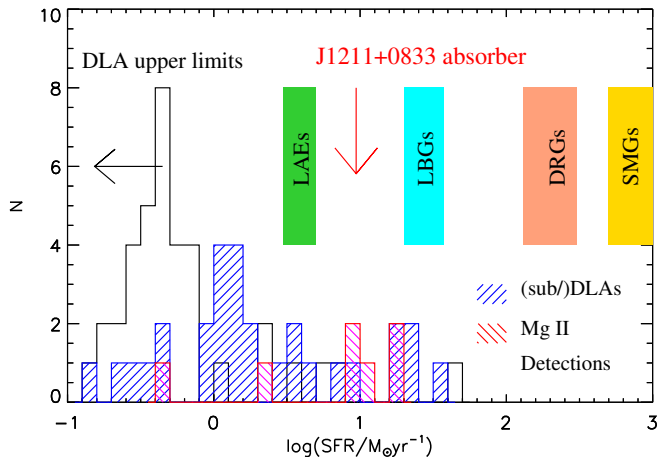


**Figure 4.** SFRs of Mg II, H I galaxies, and emission selected galaxies at  $z \sim 2-3$ . The blue, red, and black histograms show the SFRs of DLA/subDLA galaxies, Mg II galaxies, and DLA non-detections (Bouché et al. 2012; Lundgren et al. 2012; Fumagalli et al. 2015; Rahmani et al. 2016). The color bars represent the median SFRs of LAEs, LBGs, DRGs, and SMGs at similar redshifts (Reddy et al. 2006, 2010; Hagen et al. 2016). The SFR of the J1211+0833 2DA host galaxy is between those of LAEs and LBGs.

sitioning to a quiescent galaxy. The SFR and  $M_*$  of the host galaxy are comparable to though slightly lower than those of typical galaxies at  $z \sim 2$ , i.e. LBGs, BzK, UV-selected galaxies, and distant red galaxies (DRGs) (Reddy et al. 2006, 2010; Buat et al. 2012). Detecting the host galaxy at multi-wavelengths would enable a fair comparison with different emission-selected galaxy populations. It is also promising that far-infrared emission lines such as CO and C I and dust continuum emission can be detected with ALMA given their presence in absorption (Ma et al. 2015). It would be of great interest to compare its gas and dust properties to those of mid-IR and FIR/submillimeter selected galaxies, especially the polycyclic aromatic hydrocarbon (PAH) bands at mid-IR, which are considered as a promising candidate for the 2175 Å bump carriers (e.g., Draine 2003; Xiang et al. 2011).

It is worth noting that the similar redshifts of the nearby galaxies indicate a group environment. The 2175 Å bump is ubiquitous in our Milky Way Galaxy, which also resides in a group environment with multiple satellite galaxies. It is still too early to draw conclusions on whether this is a coincidence or the group environment does play a role in the formation and presence of the 2175 Å bump carriers.

## 5. SUMMARY AND CONCLUSIONS

We have detected the emission counterpart or the host galaxy of a 2DA for the first time using WFC3 IR direct imaging and grism spectroscopy. We have subtracted the quasar contamination and performed template fitting on the extracted spectrum to confirm the redshift. The spectroscopically confirmed host galaxy is located at a small impact parameter of 5.5 kpc. The morphological parameters derived from the F140W image indicate that it is a disk-like galaxy with an axis ratio of 0.73. The spectral analysis (weak [O III] and [O II] emission lines, moderate 4000 Å break and Balmer absorption lines) shows that the host galaxy contains an evolved stellar

population with small amount of current star formation. The host galaxy is found to be a chemically-enriched, evolved, massive, and star-forming disk-like galaxy that is in the transition from a blue star-forming galaxy to a red quiescent galaxy. More detections like this in the future are required to establish this population as a whole in the context of galaxy formation and evolution.

## ACKNOWLEDGMENTS

We thank the anonymous referee for the constructive comments that have improved the manuscript. J.M. is grateful to Anna Nierenburg for local technical support. This work is based on observations made with the NASA/ESA *Hubble Space Telescope* obtained at the Space Telescope Science Institute, which is operated by the Association of Universities for Research in Astronomy, Inc., under NASA contract NAS 5-26555. We acknowledge support from the *HST* GO-14200 grant. This research has made use of NASA’s Astrophysics Data System.

## REFERENCES

- Anderson, J. 2016, Space Telescope WFC Instrument Science Report
- Balogh, M. L., Morris, S. L., Yee, H. K. C., Carlberg, R. G., & Ellingson, E. 1999, *ApJ*, 527, 54
- Behroozi, P. S., Wechsler, R. H., & Conroy, C. 2013, *ApJ*, 770, 57
- Bergeron, J., & Boissé, P. 1991, *A&A*, 243, 344
- Bordoloi, R., Lilly, S. J., Hardmeier, E., et al. 2014, *ApJ*, 794, 130
- Bouché, N., Murphy, M. T., Péroux, C., et al. 2012, *MNRAS*, 419, 2
- Bouché, N., Murphy, M. T., Péroux, C., Csabai, I., & Wild, V. 2006, *MNRAS*, 371, 495
- Bouché, N., Murphy, M. T., Péroux, C., et al. 2007, *ApJ*, 669, L5
- Brammer, G. B., van Dokkum, P. G., Franx, M., et al. 2012, *ApJS*, 200, 13
- Buat, V., Noll, S., Burgarella, D., et al. 2012, *A&A*, 545, A141
- Chabrier, G. 2003, *PASP*, 115, 763
- Chen, H.-W., Helsby, J. E., Gauthier, J.-R., et al. 2010, *ApJ*, 714, 1521
- Conroy, C., & Gunn, J. E. 2010, *Astrophysics Source Code Library*, ascl:1010.043
- Conroy, C., Gunn, J. E., & White, M. 2009, *ApJ*, 699, 486
- Draine, B. T. 2003, *ARA&A*, 41, 241
- Fumagalli, M., O’Meara, J. M., Prochaska, J. X., Rafelski, M., & Kanekar, N. 2015, *MNRAS*, 446, 3178
- Fynbo, J. P. U., Prochaska, J. X., Sommer-Larsen, J., Dessauges-Zavadsky, M., & Møller, P. 2008, *ApJ*, 683, 321-328
- Hagen, A., Zeimann, G. R., Behrens, C., et al. 2016, *ApJ*, 817, 79
- Herbert-Fort, S., Prochaska, J. X., Dessauges-Zavadsky, M., et al. 2006, *PASP*, 118, 1077
- Herenz, P., Richter, P., Charlton, J. C., & Masiero, J. R. 2013, *A&A*, 550, A87
- Hernán-Caballero, A., Alonso-Herrero, A., Pérez-González, P. G., et al. 2013, *MNRAS*, 434, 2136
- Horne, K. 1986, *PASP*, 98, 609
- Jiang, P., Ge, J., Zhou, H., Wang, J., & Wang, T. 2011, *ApJ*, 732, 110
- Joshi, R., Srianand, R., Petitjean, P., & Noterdaeme, P. 2017, *MNRAS*, 471, 1910
- Kacprzak, G. G., Cooke, J., Churchill, C. W., Ryan-Weber, E. V., & Nielsen, N. M. 2013, *ApJ*, 777, L11
- Kauffmann, G., Heckman, T. M., White, S. D. M., et al. 2003, *MNRAS*, 341, 33
- Kauffmann, G., Heckman, T. M., White, S. D. M., et al. 2003, *MNRAS*, 341, 54
- Kennicutt, R. C., Jr. 1998, *ARA&A*, 36, 189
- Krogager, J.-K., Fynbo, J. P. U., Møller, P., et al. 2012, *MNRAS*, 424, L1
- Krogager, J.-K., Møller, P., Fynbo, J. P. U., & Noterdaeme, P. 2017, *MNRAS*, 469, 2959

- Krogager, J.-K., Zirm, A. W., Toft, S., Man, A., & Brammer, G. 2014, *ApJ*, 797, 17
- Krogager, J.-K., Fynbo, J. P. U., Ledoux, C., et al. 2013, *MNRAS*, 433, 3091
- Lundgren, B. F., Brammer, G., van Dokkum, P., et al. 2012, *ApJ*, 760, 49
- Ma, J., Caucal, P., Noterdaeme, P., et al. 2015, *MNRAS*, 454, 1751
- Ma, J., Ge, J., Prochaska, J. X., et al. 2018, *MNRAS*, 474, 4870
- Ma, J., Ge, J., Zhao, Y., et al. 2017, *MNRAS*, 472, 2196
- Møller, P., & Warren, S. J. 1993, *A&A*, 270, 43
- Momcheva, I. G., Brammer, G. B., van Dokkum, P. G., et al. 2016, *ApJS*, 225, 27
- Neeleman, M., Kanekar, N., Prochaska, J. X., et al. 2017, *Science*, 355, 1285
- Nielsen, N. M., Churchill, C. W., & Kacprzak, G. G. 2013, *ApJ*, 776, 115
- Nielsen, N. M., Churchill, C. W., Kacprzak, G. G., & Murphy, M. T. 2013, *ApJ*, 776, 114
- Noterdaeme, P., Krogager, J.-K., Balashev, S., et al. 2017, *A&A*, 597, A82
- Noterdaeme, P., Laursen, P., Petitjean, P., et al. 2012, *A&A*, 540, A63
- Noterdaeme, P., Ledoux, C., Srianand, R., Petitjean, P., & Lopez, S. 2009, *A&A*, 503, 765
- Peng, C. Y., Ho, L. C., Impey, C. D., & Rix, H.-W. 2010, *AJ*, 139, 2097
- Prochaska, J. X., Sheffer, Y., Perley, D. A., et al. 2009, *ApJ*, 691, L27
- Rahmani, H., Péroux, C., Turnshek, D. A., et al. 2016, *MNRAS*, 463, 980
- Rao, S. M., Belfort-Mihalyi, M., Turnshek, D. A., et al. 2011, *MNRAS*, 416, 1215
- Rauch, M., Haehnelt, M., Bunker, A., et al. 2008, *ApJ*, 681, 856-880
- Reddy, N. A., Erb, D. K., Pettini, M., Steidel, C. C., & Shapley, A. E. 2010, *ApJ*, 712, 1070
- Reddy, N. A., Steidel, C. C., Fadda, D., et al. 2006, *ApJ*, 644, 792
- Richter, P. 2012, *ApJ*, 750, 165
- Rubin, K. H. R., Prochaska, J. X., Koo, D. C., & Phillips, A. C. 2012, *ApJ*, 747, L26
- Srianand, R., Gupta, N., Petitjean, P., Noterdaeme, P., & Saikia, D. J. 2008, *MNRAS*, 391, L69
- Steidel, C. C. 1995, *QSO Absorption Lines*, 139
- Steidel, C. C., Kollmeier, J. A., Shapley, A. E., et al. 2002, *ApJ*, 570, 526
- Wang, J., Hall, P. B., Ge, J., Li, A., & Schneider, D. P. 2004, *ApJ*, 609, 589
- Wild, V., Almaini, O., Dunlop, J., et al. 2016, *MNRAS*, 463, 832
- Xiang, F. Y., Li, A., & Zhong, J. X. 2011, *ApJ*, 733, 91